COMMUNICATION

Materials for Bioresorbable Radio Frequency Electronics

*Suk-Won Hwang, Xian Huang, Jung-Hun Seo, Jun-Kyul Song, Stanley Kim, Sami Hage-Ali, Hyun-Joong Chung, Hu Tao, Fiorenzo G. Omenetto, Zhenqiang Ma, and John A. Rogers**

Devices constructed using bioresorbable materials have many roles in clinical medicine, ranging from drug delivery vehicles[1,2] to stents[3,4] and sutures.[5,6] In such cases, the function is defined primarily by the mechanics and/or the structure of the component, with operation that is often passive. The ability to achieve similar bioresorbable characteristics in active semiconductor devices and sensors could significantly expand the possible modes of use. Past approaches include partially resorbable systems based on miniaturized silicon transistors bonded to biomaterial substrates and, in separate work, on organic active materials (e.g. semiconductors).[7–11] Recent studies demonstrate a completely water soluble class of silicon-based technology,[12] to enable devices and systems that build on foundational knowledge and engineering capabilities derived from the integrated circuit industry. Components of this type can be implanted into the human body where they gradually dissolve into biofluids after their useful functional life, thereby eliminating unnecessary device load without the need for surgical extraction. For many applications, radio frequency (RF) operation is a key feature, both for data transmission and for power supply. The results presented here represent progress in this direction. We report antennas, rectifying diodes, transistors, capacitors, inductors, resistors, ring oscillators and RF energy harvesting sub-systems, all of which involve water soluble and biocompatible constituent materials, i.e. silicon nanomembranes (Si NMs; semiconductors), magnesium (Mg; conductors), silicon dioxide or magnesium oxide (low temperature SiO_2 or MgO; interlayer dielectrics), and silk (substrates).

One of the most critical, but simplest, elements in RF systems for wireless reception/transmission is in the antenna. Transient antennas can be formed by evaporation of Mg (500 nm) through stencil masks made of polyimide (PI) films (Kapton, 12.5 μm, Dupont, USA) on thin films of silk. Two designs form the focus of studies reported here: simple linear dipoles consisting of two quarter wavelength arms and wideband quasi log-periodic dipoles, designed to operate at ~2.4 GHz and ~950 MHz, respectively. **Figure 1**a presents images of a transient Mg antenna at a sequence of times during immersion in deionized (DI) water at room temperature. The Mg and silk completely disappear after ~2 hours by hydrolysis and simple dissolution, respectively. An alternative route to similar antennas, but with thicknesses that can be much larger than the skin depth at relevant RF frequencies, exploits Mg foils (thickness from 5 μm to 50 μm, purity of 99.9%, Goodfellow, UK) cut into appropriate shapes. A layer of solvent-perfused silk serves as an adhesive to bond such antennas to silk substrates (Figure S1a). The measured S-parameters in Figure 1b show that both antennas are well matched to their designed operating frequencies. Images of the devices with coaxial connectors appear in Figure S2. Figure S1b shows a 950 MHz antenna integrated with a commercial RF power scavenging system on a printed circuit board to demonstrate functionality. Additional details can be found in Figure S1c.

Various transient devices with passive RF function, such as capacitors, inductors, and resistors, are also essential. Figure 1, c to g, provides images and electrical properties of several such components. As an example, a simple transient resistor consisting of a serpentine trace of Mg (Figure 1c) formed by evaporation onto silk through a stencil mask, indicates a resistance of 100 ohm, suitable for use in RF current-limiters and voltage dividers. Capacitors and inductors can be formed on silk in which MgO (900 nm thick, formed by electron beam evaporation) serves as the dielectric, and Mg forms the electrodes and conducting traces. (Details appear in the experimental section.) The capacitors explored here exploit simple, parallel plate geometries with various lateral dimensions (Figure 1d; 150 μm × 150 um (black), 250 μm × 250 μm (red), 400 μm × 400 μm (blue) and 550 μm × 550 μm (green)). Measured capacitances and Q factors of each capacitor appear in Figure 1e, along with simulation results. The operating frequencies extend up to ~6 GHz. Simple inductors (Figure 1f)

S.-W. Hwang, Dr. X. Huang, S. Kim, Dr. S. Hage-Ali, Dr. H.-J. Chung
Department of Materials Science and Engineering
Frederick Seitz Materials Research Laboratory
University of Illinois at Urbana-Champaign
Urbana, IL 61801, USA
E-mail: jrogers@illinois.edu
J.-H. Seo, Prof. Z. Ma
Department of Electrical and Computer Engineering
University of Wisconsin-Madison
Madison, WI 53706, USA
J.-K. Song
Department of Chemistry
University of Illinois at Urbana-Champaign
Urbana, IL 61801, USA
Dr. H. Tao, Prof. F. G. Omenetto
Department of Biomedical Engineering
Tufts University
Medford, MA 02155, USA
Prof. J. A. Rogers
Department of Materials Science and Engineering Chemistry
Mechanical Science and Engineering
Electrical and Computer Engineering
Beckman Institute for Advanced Science and Technology
and Frederick Seitz Materials Research Laboratory
University of Illinois at Urbana-Champaign
Urbana, IL 61801, USA
E-mail: jrogers@illinois.edu

DOI: 10.1002/adma.201300920

© 2013 WILEY-VCH Verlag GmbH & Co. KGaA, Weinheim

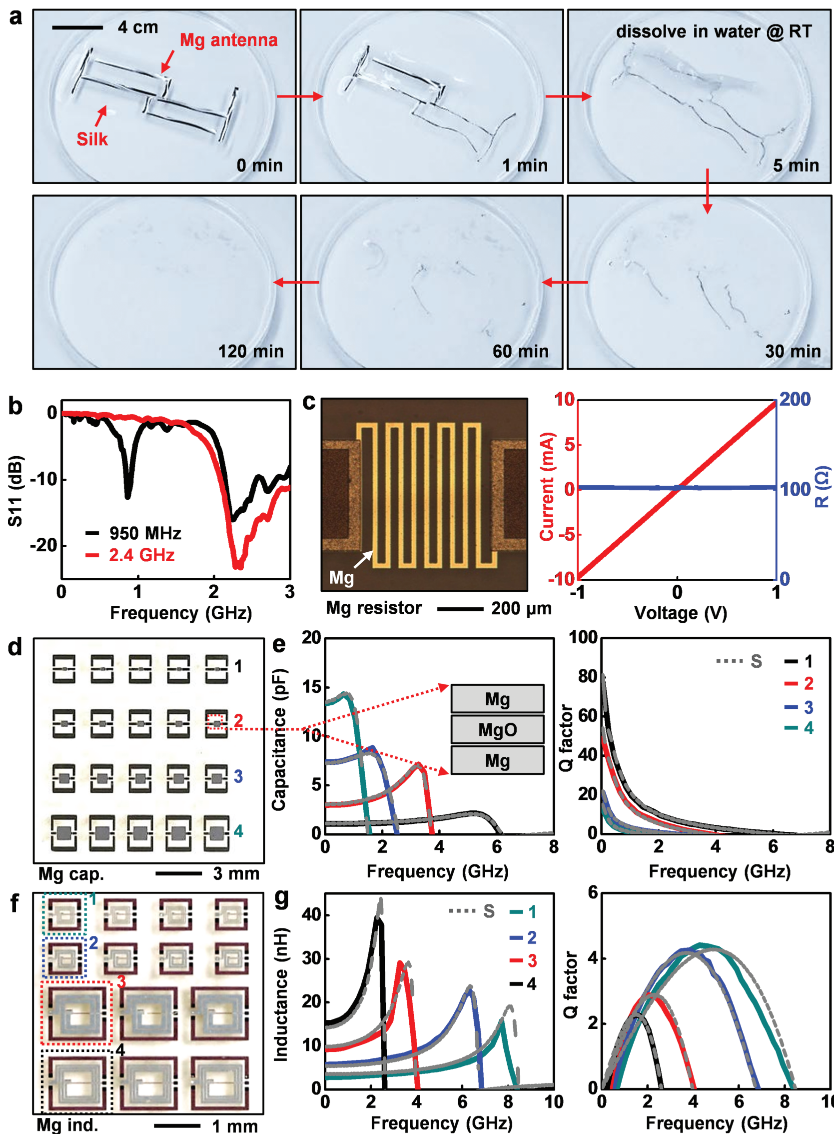

Figure 1. Images and electrical properties of various passive components for transient RF systems: (a) A set of images of an antenna built with Mg on a silk substrate illustrates the process of dissolution in DI water. The Mg disappears completely by hydrolysis within ~2 hours. (b) Measured reflection coefficient S11 of Mg antennas operating at 950 MHz and 2.4 GHz. (c) Optical microscope image of a Mg resistor (left), and its current-voltage characteristics (right). The resistance is ~100 ohm. (d) Image of capacitors of different sizes built using Mg electrodes and MgO dielectrics. (e) Measured capacitance (left) and Q factor (right) as a function of frequency. Experimental results and simulations appear as lines and dots, respectively. The region of overlap between the top and bottom Mg electrodes in these metal-insulator-metal (MIM) capacitors is 150 µm × 150 um (black), 250 µm × 250 µm (red), 400 µm × 400 µm (blue) and 550 µm × 550 µm (green). The inset provides a schematic illustration of a device. (f) Image of a collection of inductors that use Mg electrodes and MgO for interlayer dielectrics. The number of turns (*n*), outer diameter (*d*) and metal width/space (*w*/*s*) are 3, 440 µm, 20/20 µm (green), 2, 440 µm, 40/20 µm (blue), 2, 1 mm, 100/20 µm (red), 3, 1 mm, 50/20 µm (black). (g) Measured inductance (left) and Q factor (right) as a function of frequency up to ~8 GHz for four representative inductors. Experimental results and simulations appear as lines and dots, respectively.

can be built using planar spiral coils with 2 or 3 turns; connections to the inner terminals use MgO (900 nm) as an interlayer dielectric. These devices have different resonance and maximum operating frequencies (Figure 1g, from 2 GHz to 8 GHz). The Q factors are modest, but can be improved by increasing the thickness of the Mg. Additional measurements and simulations on capacitors and inductors appear in Figure S3 to S5. Electrical behaviors in capacitors and inductors can be captured quantitatively using equivalent circuit models and parameters. Here, the devices are represented by a combination of main and parasitic parameters, such as inductances, capacitances, and resistances, that yield a good match with the measured characteristics. The circuit simulations use these device models.

Most RF circuits demand semiconductor devices. **Figure 2**a presents a schematic illustration of structures for transient RF silicon PIN diodes that use Mg contacts to silicon nanomembranes (Si NMs, thickness ~300 nm, p-type) with heavily doped p-type and n-type regions separated by lightly doped, nearly intrinsic areas. The fabrication involves patterned boron and phosphorous doping (950 °C ~ 1050 °C) of Si NMs while they are supported on a silicon wafer. Transfer printing delivers the Si NMs onto a film of silk cast on a separate wafer. Electron beam evaporation of Mg (~400 nm thickness) through a fine-line stencil mask aligned to the doped regions of the Si NMs defines the contacts and interconnects. (Details appear in the experimental section.) Electrical measurements of a representative device (length and width of the intrinsic region: 5 µm and 1 ~ 2 mm, respectively) in Figure 2b indicate expected diode behavior, with a turn-on voltage at ~0.7 V and a forward current of ~1.5 mA at 1 V (left). Operation as a rectifier extends to a few GHz (right). Output responses to alternating current inputs at various frequencies, and measurements and simulations of the S-parameters appear in Figure S6 and S7. Figure 2c illustrates the dissolution kinetics of similar diodes fabricated on a glass substrate, encapsulated by a uniform layer of MgO (~500 nm thickness), and partially immersed in deionized (DI) water at room temperature. The measured electrical properties indicate stable operation for ~4 hours, followed by rapid degradation in ~45 minutes. The first stage of this kinetics depends on dissolution of the MgO encapsulant and/or permeation through it; the second depends mainly on hydrolysis of the Mg electrodes. The thickness of the MgO can be selected to define the first time scale, in a way that does not affect device performance. Other encapsulating materials can be considered for times that extend beyond those practically accessible with MgO.[12]

© 2013 WILEY-VCH Verlag GmbH & Co. KGaA, Weinheim

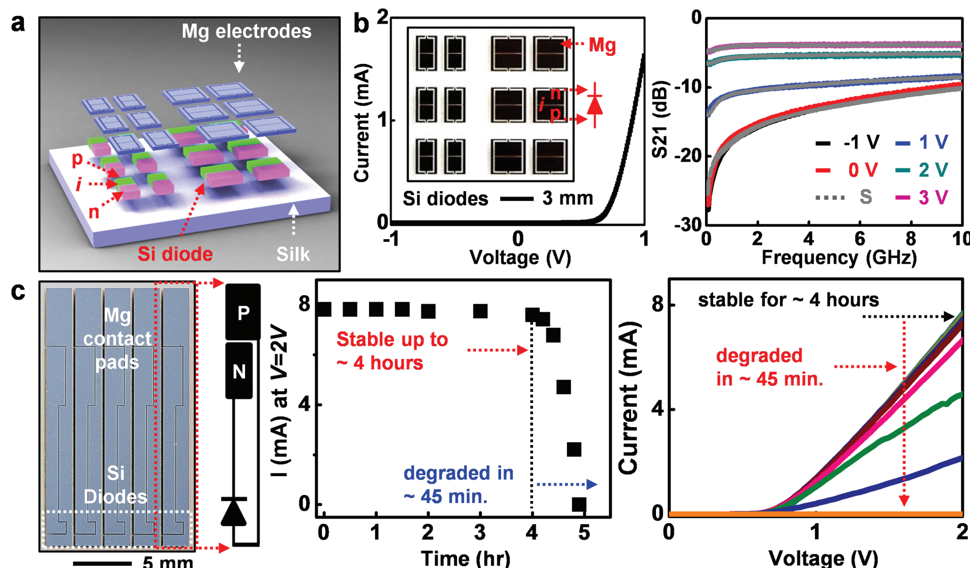

Figure 2. Electrical measurements of transient diodes, and dissolution kinetics of a representative diode and antenna: (a) Schematic illustration of Si NM PIN diodes (rectifiers) fabricated with Mg electrodes on a silk substrate. The near intrinsic "*i*" region has dimensions of ~5 μm × 1 ~ 2 mm. (b) Current-voltage characteristics of a representative diode (left), including an image in the inset, and measured values (lines) and simulations (dots) of the S21 scattering parameter at frequencies up to 10 GHz with different DC biases (right). (c) Measurements of dissolution kinetics of a diode encapsulated with MgO (~500 nm). The results show stable current output for ~4 hours, followed by rapid degraded over the following ~45 min. due to dissolution of the Mg electrodes.

RF transistors enable active functionality. To demonstrate possibilities in transient RF, we constructed three-stage complementary metal-oxide-semiconductor (CMOS) ring oscillators using transient n-channel and p-channel metal-oxide-semiconductor field-effect transistors (MOSFETs) based on Si NMs, with Mg (~250 nm) for source, drain, gate contacts and interconnects, and MgO (~80 nm) for the gate dielectrics. **Figure 3**a provides an illustration and a schematic circuit diagram. To enable both n- and p-channel MOSFETs in a single Si NM, high temperature diffusion procedures create lightly doped p-wells (p^-), and highly doped source and drain contacts for each MOSFET (n^+, p^+). Source and drain electrodes formed next to the p-wells define p-channel MOSFETs. Heavily doped regions for source and drain regions inside the p-wells enable contacts for n-channel MOSFETs. (See details in experimental section.) Figure 3b and 3c represent transfer curves and full current-voltage characteristics measured from p-channel and n-channel devices, respectively. Optical microscope images appear in the insets. In both types of MOSFETs, the on/off current ratios (I_{on}/I_{off}) are ~10^5. The mobilities are ~70 $cm^2/V \cdot s$ and ~350 $cm^2/V \cdot s$, for the p- and n-channel cases, respectively. Measurements on a typical CMOS inverter appear in Figure 3d; the gain and threshold voltage (V_{th}) are ~60 and –1 V, respectively. The negative threshold voltage of the inverters results mainly from the high negative threshold voltage (~5 V) of the p-channel MOSFETs. Figure 3e shows time-domain output voltage characteristics of a ring oscillator. The operating frequency can be adjusted, up to ~4.1 MHz, with applied bias, 10 V (black), 15 V (red), 20 V (blue). Theoretically, this frequency is inversely proportional to the number of stages (N) and linearly proportional to the applied voltage (V_{dd}). In the absence of other factors, the relative slope is expected to be approximately 1. Deviations from this behavior suggest some non-idealities, likely due to propagation delays and parasitic capacitances.[13,14]

The various transient RF electronic devices described previously can be integrated together for higher levels of functionality. A transient wireless RF power scavenger circuit provides a good example (**Figure 4**). The circuit contains an RF antenna, an inductor, six capacitors, a resistor and eight diodes, as shown in Figure 4a-b. A circuit diagram appears in Figure 4c. In this case, a thin layer of polyimide provides mechanical support to facilitate transfer of the entire, interconnected system (except for the antenna) to silk at improved yields. Connecting the input of the system to an RF function generator and the output to a commercial LED indicates effective rectification, over a frequency range from 10 kHz to 950 MHz (Figure 4d). Additional data appear in Figure S7e. By connecting the circuit to a Mg antenna designed for operation at 950 MHz, the system can wirelessly harvest energy from an RF transmitter, to turn on a LED at a distance of ~2 meters, as shown in Figure 4e. The power received by the antenna is approximately 17.3 dBm (54 mW) and the LED consumes a power of 8.5 mW. The resulting power conversion efficiency (PCE) is determined to be -8 dB (15.7%). This value is somewhat smaller than those of commercial bridge rectifiers, which range from 26.5% to 37%, due to their use of optimized fabrication processes and materials.[15–17] Systems based on half-wave rectification circuits can also power LEDs, but with reduced efficiencies compared to the case of the full-wave rectifier (Figure S8). Circuits designed to enable integration with Si CMOS ring oscillators powered by scavenging circuits appear in Figure S9. In all examples, the electronic materials are water-soluble/biodegradable. Figure 4f shows a set of images collected at different times during dissolution. The entire power scavenger initially disintegrates in DI water at room temperature due to dissolution of the silk substrate; subsequently,

© 2013 WILEY-VCH Verlag GmbH & Co. KGaA, Weinheim

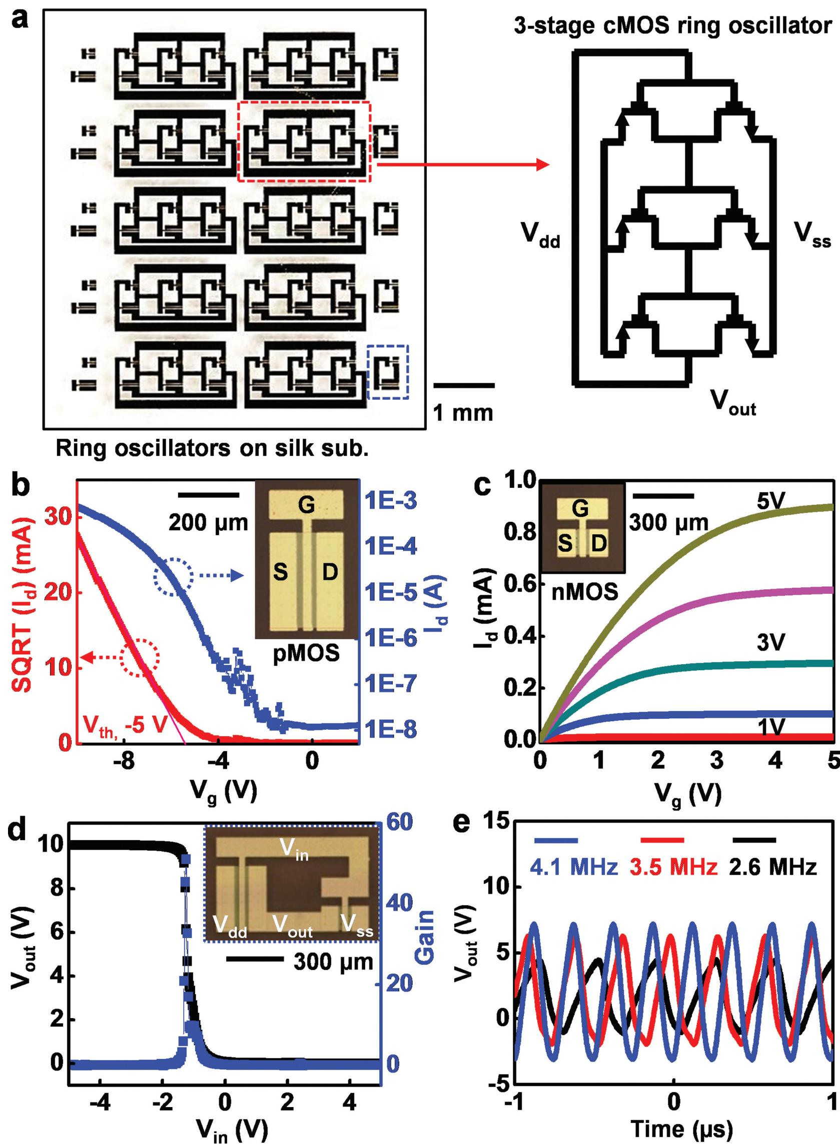

Figure 3. Images and measured properties of transient CMOS inverters and ring oscillators: (a) Image of CMOS three-stage ring oscillators (left), and circuit diagram (right). (b) SQRT (red) and log scale (blue) transfer curves of a typical transient p-channel MOSFET. The channel length (L) and width (W) are 5 µm and 300 µm, respectively. The mobility and on/off ratio are ~70 $cm^2/V \cdot s$ and ~10^5, respectively. The inset shows a microscope image of a representative device. (c) *I–V* characteristics of a typical n-channel MOSFET. The channel length (L) and width (W) are 15 µm and 100 µm, respectively. The mobility and on/off ratio are 350 $cm^2/V \cdot s$ and ~10^5, respectively. All MOSFETs use Mg for source, drain and gate electrodes, and MgO for the gate dielectric. (d) Output voltage characteristics of a representative CMOS inverter with V_{dd} = 10 V. The voltage gain is ~60. An optical microscope image appears in the inset. (e) Measured time domain responses of a ring oscillator at different frequencies.

the remaining materials reactively dissolve at their respective rates. A thick layer of Mg (~3 µm) requires some days to dissolve. At these neutral pH levels, the Si and the low temperature SiO_2 formed by plasma-enhanced chemical-vapor deposition (PECVD) dissolve at rates that are much slower than those at physiological conditions.[12] (Under such conditions, thermal SiO_2 dissolves at rates that are negligibly small)

In summary, the materials, device designs and manufacturing strategies described here provide a baseline of components for RF transient electronics. The results demonstrate the versatility of the constituent materials and associated fabrication processes, and provide building blocks that are essential to many envisioned uses of transient technologies, particularly in wireless power delivery and communication approaches for implantable medical devices and environmental monitors.

Experimental Section

Fabrication of transient passive components (capacitors and inductors): Mg electrodes (~200 nm) for bottom contacts (capacitors) and crossovers (inductors) were formed by electron beam evaporation on a silk substrate. Deposition of MgO (~900 nm) defined interlayer dielectrics. Another layer of Mg served as top electrodes for capacitors (~1 µm), and planar spiral coils for inductors (~3 µm). In all cases, high resolution stencil masks made of polyimide (PI) films (Kapton, 12.5 µm, Dupont, USA) were used to pattern the Mg and MgO.

Fabrication of transient Si CMOS ring oscillators: Three different doping procedures were performed on an n-type SOI wafer (SOITEC, France). Boron doping at 550 °C using spin-on dopant (SOD, Filmtronics, USA) defined lightly doped regions for the p-wells (p-). Heavily doped p-type regions for source and drain electrodes were formed at 1050 °C for p-type transistors. Phosphorous doping at 950 °C defined highly doped areas for source and drain contacts for n-type transistors. These doped silicon nanomembranes (Si NMs) were isolated by reactive ion etching (RIE; Plasmatherm) with sulfur hexafluoride (SF_6) gas. To release the Si NMs from the SOI, the buried oxide was partially removed by wet etching with hydrofluoric acid (HF, 49% electronic grade, ScienceLab, USA). Next, patterning a layer of photoresist (AZ 5214) formed structures that anchored the Si NMs to the underlying wafer during a second etching step to complete the removal of the buried oxide. Individual Si NMs formed by this procedure were transfer printed onto a temporary "carrier" substrate coated with a layer of silk. Gate dielectrics (MgO, ~80 nm), as well as electrodes and interconnects (Mg, ~300 nm) were deposited by electron-beam evaporation through fine-line stencil masks.

Fabrication of transient RF power scavenger systems: High temperature diffusion doping of boron at ~1050 °C and phosphorous at ~950 °C using spin-on dopant established desired patterns of doping in the top silicon layer of a silicon-on-insulator (SOI, SOITEC, France) substrate. Thermally grown oxide (~1100 °C) served as the doping mask. Removal of the buried oxide layer (~1 µm) with HF, released doped Si NMs (thickness ~300 nm, p-type), for transfer printing onto a carrier wafer coated with poly (methylmethacrylate) (PMMA, ~100 nm; sacrificial) and polyimide (PI, ~1.2 µm; cured at 250 °C for 1 hour in a glove box). Active device regions were isolated by RIE with SF_6 gas. The first layer of electrodes/interconnects was defined by lift-off using LOR 20B (Microchem, USA) and AZ 5214 photoresists, with Mg (150 nm) deposited by electron beam evaporation. A 900 nm thick layer of SiO_2 was deposited by low temperature plasma-enhanced chemical-vapor deposition (PECVD). Openings to the contacts were formed by

© 2013 WILEY-VCH Verlag GmbH & Co. KGaA, Weinheim

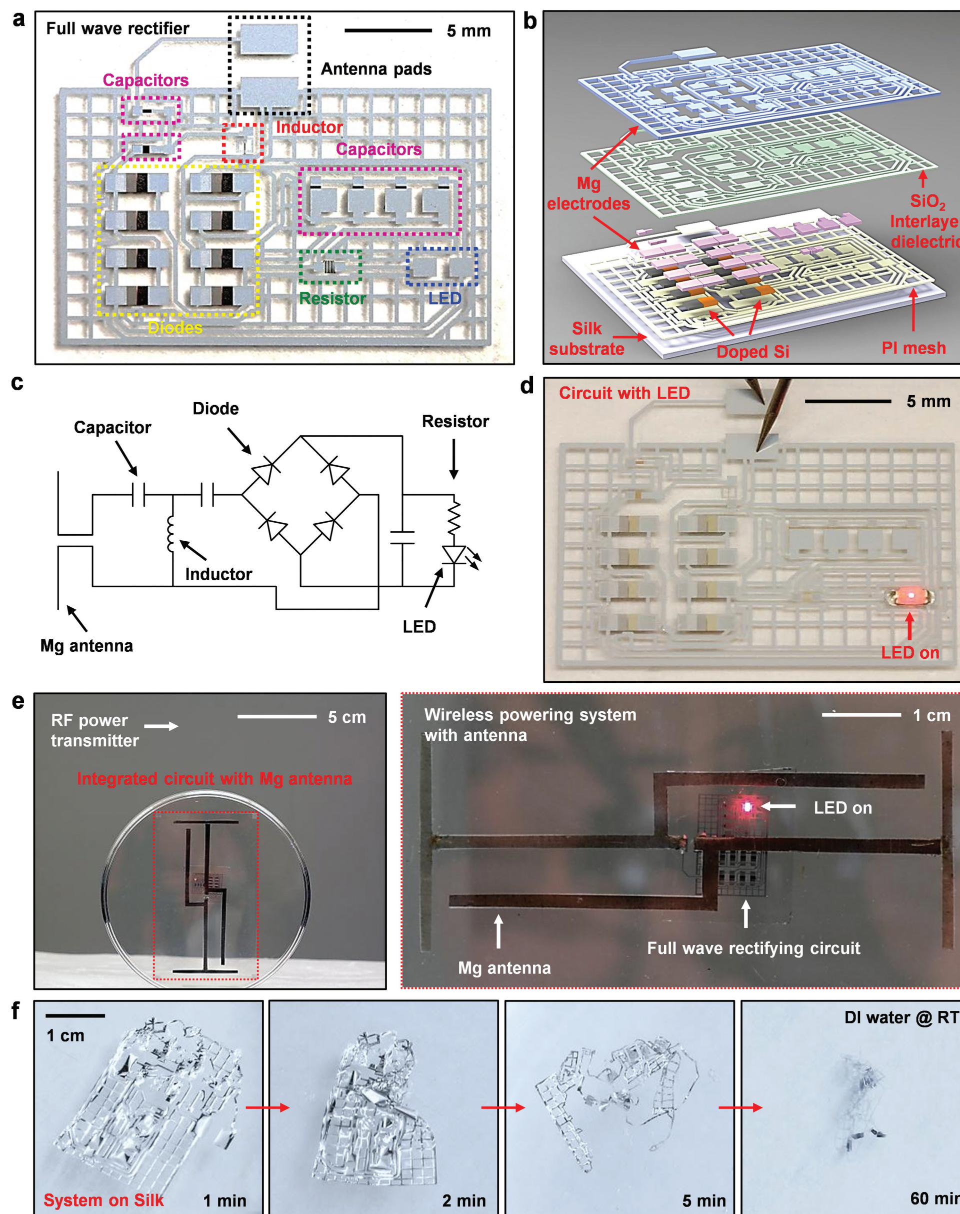

Figure 4. Transient RF power scavenging circuits, and integration with a transient antenna: (a) Image of transient full-wave rectifying circuit that includes an array of diodes and capacitors, an inductor, a resistor and antenna pads, all fabricated with transient electronic materials: Si NMs (semiconductors), Mg (electrodes), SiO_2 (interlayer dielectrics), and silk (substrates). (b) Schematic exploded view illustration. (c) Circuit diagram. (d) Operational demonstration of a full wave rectifying circuit with a commercial LED. (e) Image of a full wave rectifying system powered wirelessly with an RF transmitter and a Mg receiving antenna (left), and magnified view (right). The working distance here is ~2 meters. (f) Images of a rectifying circuit immersed in deionized water after 1 min, 2 min, 5 min and 1 hour, respectively.

buffered oxide etching (BOE, 6:1, Transene company, USA) of the SiO_2. Photolithography (AZ nLOF 2070, Microchem, USA) and liftoff with a thick film of Mg (~3 µm) defined the second layer of electrodes/interconnects. Next, an oxygen RIE (March) step created an open mesh pattern in the PI to allow removal of the PMMA by immersion in acetone. Entire devices released in this manner were then transfer printed onto a film of silk.

RF electrical characterizations: Each passive component was measured for scattering (S-) parameters using an Agilent E8364A performance network analyzer. An external DC power supply was applied to the diodes using a bias-tee during testing. The measurement setup was calibrated to the probe tips using a standard Short-Open-Load-Thru (SOLT) on-wafer probing kit for a frequency range of 45 MHz—20 GHz. Agilent Advanced Design System (ADS) was used to extract device model parameters from the respective equivlent circuits. The antennas were connected to SubMiniature - A (SMA) connectors with silver epoxy. Their impedance characteristics were measured using an Agilent 5062A network analyzer with 1-port Open-Short-Load calibration.

Supporting Information

Supporting Information is available from the Wiley Online Library or from the author.

© 2013 WILEY-VCH Verlag GmbH & Co. KGaA, Weinheim

Acknowledgements

S. -W. H. and X. H. contributed equally to this work. This material is based upon work supported by the Defense Advanced Research Projects Agency. J.-H. Seo and Z. Ma are supported by AFOSR MURI under grant FA9550-08-1-0337.

Received: February 27, 2013
Published online: May 17, 2013

[1] K. R. Kamath, K. Park, *Adv. Drug Delivery Rev.* **1993**, *11*, 59.
[2] K. S. Soppimatha, T. M. Aminabhavia, A. R. Kulkarnia, W. E. Rudzinski, *J. Controlled Release* **2001**, *70*, 1.
[3] M. Peuster, P. Wohlsein, M. Brügmann, M. Ehlerding, K. Seidler, C. Fink, H. Brauer, A Fischer, G. Hausdorf, *Heart* **2001**, *86*, 563.
[4] M. Moravej, D. Mantovani, *Int. J. Mol. Sci.* **2011**, *12*, 4250.
[5] J. P. Singhal, H. Singh, A. R. Ray, *Polym. Rev.* **1998**, *28*, 475.
[6] A. Lendlein, R. Langer, *Science* **2002**, *296*, 1673.
[7] D.-H. Kim, Y.-S. Kim, J. Amsden, B. Panilaitis, D. L. Kaplan, F. G. Omenetto, M. R. Zakin, J. A. Rogers, *Appl. Phys. Lett.* **2009**, *95*, 133701.
[8] D.-H. Kim, J. Viventi, J. Amsden, J. Xiao, L. Vigeland, Y.-S. Kim, J. A. Blanco, B. Panilaitis, E. S. Frechette, D. Contreras, D. L. Kaplan, F. G. Omenetto, Y. Huang, K.-C. Hwang, M. R. Zakin, B. Litt, J. A. Rogers, *Nat. Mater.* **2010**, *9*, 511.
[9] C. J. Bettinger, Z. Bao, *Adv. Mater.* **2010**, *22*, 651.
[10] M. Irimia-Vladu, P. A. Troshin, M. Reisinger, L. Shmygleva, Y. Kanbur, G. Schwabegger, M. Bodea, R. Schwödiauer, A. Mumyatov, J. W. Fergus, V. F. Razumov, Helmut Sitter, N. S. Sariciftci, S. Bauer, *Adv. Funct. Mater.* **2010**, *20*, 4069.
[11] C. Legnani, C. Vilani, V. L. Calil, H. S. Barud, W. G. Quirino, C. A. Achete, S. J. L. Ribeiro, M. Cremona, *Thin Solid Films*, **2008**, *517*, 1016.
[12] S.-W. Hwang, H. Tao, D.-H. Kim, H. Cheng, J.-K. Song, E.Rill, M. A. Brenckle, B. Panilaitis, S. M. Won, Y.-S. Kim, Y. M. Song, K. J. Yu, A. Ameen, R. Li, Y. Su, M. Yang, D. L. Kaplan, M. R. Zakin, M. J. Slepian, Y. Huang, F. G. Omenetto, J. A. Rogers, *Science*, **2012**, *337*, 1640.
[13] M. K. Mandal, B. C. Sarkar, *Indian J. Pure Appl. Phy.* **2010**, *48*, 136.
[14] V. Michal, *Radioelektronika 2012 22nd International Conference*, **2012**, 1.
[15] J. Yi, W.-H. Ki, C.-Y. Tsui, *IEEE T. Circuits Syst.* **2007**, *54*, 153.
[16] P. T. Theilmann, C. D. Presti, D. Kelly, P. M. Asbeck, *Proc. IEEE Radio Frequency Integrated Circuits Symp.* **2010**, 105.
[17] P. T. Theilmann, C. D. Presti, D. J. Kelly, P. M. Asbeck, *IEEE T. Circuits Syst.* **2012**, *59*, 2111.

© 2013 WILEY-VCH Verlag GmbH & Co. KGaA, Weinheim